



LAWRENCE
LIVERMORE
NATIONAL
LABORATORY

PoP from APS talk - Measuring Characteristic Differences between High- and Low-Performing Discharges on the MegaJoule Neutron Imaging Radiography (MJOLNIR) DPF

A. Schmidt, C. Goyon, A. Link, E. Anaya, G. Bartolo, P. Cambell, S. Chapman, C. Cooper, D. Max, M. McMahon, Y. Podpaly, A. Povilus

February 8, 2022

Physics of Plasmas

Disclaimer

This document was prepared as an account of work sponsored by an agency of the United States government. Neither the United States government nor Lawrence Livermore National Security, LLC, nor any of their employees makes any warranty, expressed or implied, or assumes any legal liability or responsibility for the accuracy, completeness, or usefulness of any information, apparatus, product, or process disclosed, or represents that its use would not infringe privately owned rights. Reference herein to any specific commercial product, process, or service by trade name, trademark, manufacturer, or otherwise does not necessarily constitute or imply its endorsement, recommendation, or favoring by the United States government or Lawrence Livermore National Security, LLC. The views and opinions of authors expressed herein do not necessarily state or reflect those of the United States government or Lawrence Livermore National Security, LLC, and shall not be used for advertising or product endorsement purposes.

Measuring Characteristic Differences between High- and Low-Performing Discharges on the MegaJoule Neutron Imaging Radiography (MJOLNIR) DPF

A. Schmidt^{1*}, C. Goyon¹, A. Link¹, C. Cooper¹, R. Anaya¹, M. Anderson¹, G. Bartolo¹, P. C. Campbell¹, S. Chapman¹, D. Max², M. McMahon¹, Y. A. Podpaly¹, A. Povilus¹

¹Lawrence Livermore National Laboratory, Livermore, California 94550, USA

²National Nuclear Security Site, North Las Vegas, Nevada 89030, USA

Abstract

A dense plasma focus (DPF) is a compact coaxial plasma gun which completes its discharge as a Z-pinch, producing short (<100 ns) pulses of ions, X-rays, and/or neutrons. LLNL recently constructed and began operating a new device, the MJOLNIR (MegaJoule Neutron Imaging Radiography) DPF, which is designed for single-pulse flash neutron radiography. This device has achieved neutron yields of up to 4.1×10^{11} neutrons/pulse at 3.3 MA peak current and higher-current commissioning is underway. Like most DPFs, MJOLNIR exhibits variable yields in some configurations. We present evidence of the role of parasitic current paths within the gun in stochastically influencing the yield. First through “conditioning shots,” where new hardware has been introduced, we show that increased run-down and run-in speeds correlate with higher yields. These observations are consistent with current being delivered to the electrodes but not to the main plasma sheath, degrading the implosion-driving force. Once nominal conditions are established, we correlate low-performing discharges with smaller current dip and associated voltage spike for a fixed machine configuration. A snow-plow model is able to recreate small-magnitude current dips through the introduction of a parasitic current path and particle-in-cell simulations establish how parasitic current paths lower the ion beam energy available to produce neutrons. Finally, we observe an increased likelihood of shots with low yield and smaller current dip with increasing fill pressure.

of plasma current, with neutron production generally increasing as plasma current increases.

I. Introduction

The dense plasma focus (DPF) [1] is a coaxial plasma rail gun whose plasma discharge ends in a Z-pinch configuration. At the beginning of the discharge, the fill gas flashes over across the insulator, creating a conducting plasma sheath. The plasma sheath is accelerated down the length of the gun and then inward towards the axis by a self-generated magnetic field. Finally, the plasma current sheath pinches on axis, and eventually breaks up due to instabilities, dramatically increasing the plasma impedance leading to a large electric field across the broken-up plasma column. When operated with a deuterium or deuterium-tritium (DT) gas fill, a DPF produces a short pulse (typically <100 ns) of neutrons through energetic ion collisions. DPFs can be scaled from several kA of plasma current to several MA

The MegaJoule Neutron Imaging Radiography (MJOLNIR) DPF [2] was designed and built at Lawrence Livermore National Laboratory (LLNL) for the purpose of developing a viable neutron source for flash neutron radiography. Many DPFs, including MJOLNIR, have demonstrated variable neutron yield with nominal identical starting conditions [3]. These variations can be somewhat small, like factors of two, or dramatic, such as an order of magnitude or more variation. We present an initial effort to understand the characteristic differences between shots of different yield on MJOLNIR, using snow-plow and particle-in-cell (PIC) modeling [4-7], and a suite of diagnostics. Typically, dramatically different yields occur during electrode conditioning or other known abnormal conditions, while a factor of two

* Corresponding author, schmidt36@llnl.gov

fluctuation in yield from a nominal value is typical during normal operations.

We have several tools to understand what may be causing these fluctuations in yield. We use fiber-coupled photodiodes [2] and an optical framing camera to measure plasma sheath velocity, which is one manifestation of the total current flowing through the sheath. We do not at present have a direct measurement of current flowing through the plasma sheath, so we use Rogowski coil measurements of current flowing into the DPF head in combination with snow-plow modeling to interpret shot-to-shot differences in the current trace during the implosion phase. More detailed PIC modeling is used to understand what happens to the ion beam and neutron yield when plasma current is diverted from the plasma sheath to another conducting path.

Here we distinguish between a few different mechanisms at that can affect the yield of the DPF. The DPF yield can initially be low after a vacuum break, especially if the vacuum chamber has been exposed to the atmosphere for several days or new hardware has been introduced to the chamber, and usually improves with electrode conditioning. We present measured changes in plasma velocity during conditioning in section III B. DPF yields can also be highly variable in known off-normal conditions, such as a significant contamination of the chamber, and we correlate low-yield shots in these circumstances with changes in plasma run-in velocity in section III C. DPF yields may also fluctuate shot to shot. When yield fluctuates by factors of 2 or less from a nominal value, we consider this to be favorable operating conditions, and our velocity measurements are usually not sensitive enough to correlate with these smaller fluctuations in yield. However, these yield fluctuations still correlate with dips on current traces and the anode-cathode voltage during the pinch, which is discussed in section III D.

Finally, it is documented that MA-class DPFs exhibit a cessation of yield above a certain current or stored energy, typically several 100s kJ [8]. So far we have not run into a limit like this on MJOLNIR but we document initial observations during commissioning in the upgraded pulsed power configuration. In particular, high-pressure shots more frequently exhibit the same current trace signatures of low-yield discharges.

Observations on high pressure shots are discussed in section III F.

II. Methods and Materials

A. MJOLNIR

MJOLNIR (Fig. 1) is a DPF intended to be optimized for flash neutron radiography. From August 2018 to December 2019, MJOLNIR was operated with a maximum of 1 MJ of stored energy capacity. The stored energy capacity was subsequently doubled to 2 MJ in January 2020, although as of the time of writing, it had only been commissioned to 1 MJ (70% of max voltage) in this configuration.

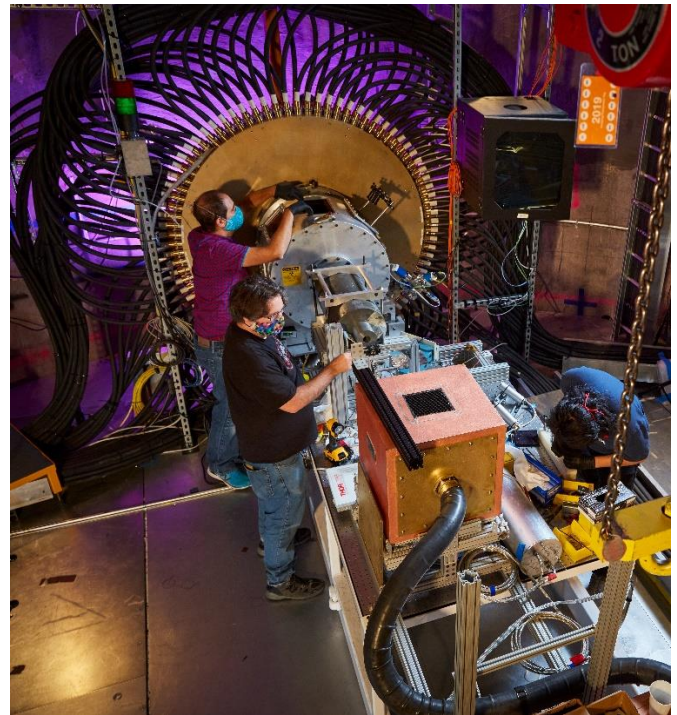


Figure 1: The MJOLNIR DPF head (in the 2-MJ configuration/168 transmission cables), and neutron imaging camera. The pulsed power driver is located one level below.

The 1-MJ (2-MJ) configuration of the MJOLNIR pulsed power driver is composed of three (six) 4.9 m-tall air-pressure-insulated Marx towers (Fig. 2) that house 12 (24) single-stage Marx modules. Each Marx module consists primarily of two 34 μF capacitors and a single high-current railgap switch, both from the decommissioned Atlas experiment [9-11]. The Marx towers generate a voltage and current pulse which is

transferred via 84 (168) flexible transmission line cables to a radial transmission plate and ultimately to the DPF head and dynamic plasma load.

In the 1-MJ configuration, the plasma current reaches up to 2.5 MA when the system is charged to +/-50 kV (i.e. 100 kV erected). In the 2-MJ configuration, MJOLNIR has been commissioned to +/-35 kV (i.e. 70 kV erected) so far, reaching currents up to 3.25 MA. The increase in the peak current from the first configuration at 100 kV to the second at 70 kV is primarily due to the lowered gun inductance when the anode radius is increased by 50% but the AK gap remains constant. It is important to note that although the 2-MJ configuration of MJOLNIR is capable of 2-MJ stored energy at maximum voltage (100 kV), at the time of the writing of this paper, it has only been commissioned to 1 MJ at 70 kV. The highest neutron yields achieved to date are 3.8×10^{11} in the 1-MJ configuration and 4.1×10^{11} in the 2-MJ configuration.



Figure 2: Two of MJOLNIR's six pulsed power pressurized towers.

In the 1-MJ configuration, measured lumped circuit parameters for the the bank, cables, and transmission plate are 204 μF capacitance, 67.4 nH inductance and 12.5 mOhm resistance.

Although a hard short test has not yet been conducted in the 2-MJ configuration, estimates of lumped circuit parameters have been obtained through a comparison of measured current traces to snow-plow modeled current traces. Estimated lumped circuit parameters for the bank, including protective resistors is 408 μF

capacitance, with 46.7 nH inductance and 6.3 mOhm resistance.

Diagnostics included in the study are as follows: A Be activation neutron detector measures the DPF yield [2]. The main head Rogowski coil measures the time trace of the current in the head [2] and a voltage probe independently measures the anode-cathode voltage at the transmission plate. Fiber-coupled photodiode detectors measure the timing of the plasma sheath as it sweeps past a fixed location on the anode during the run-down phase [2]. A 16-frame camera measures the visible light emitted by the sheath when it reaches the anode tip. Each frame corresponds to 3 ns exposures that are independently amplified and can be arbitrarily spaced in time.

The voltage across the transmission plate is measured using an inductively coupled voltage probe consisting of a 100 kV, 955.5 Ohm solid carborundum resistor surrounded by an 8 nH Rogowski coil with 50 MHz bandwidth, frequency-corrected up to 200 MHz using a network analyzer. The resistor inductance is sufficiently low that the simplified Ohm's law can be adopted to convert the current through the resistor into the voltage across the transmission plate. An inductively coupled measurement was selected for its ability to deliver high fidelity signals faster than the characteristic frequency of the DPF voltages while still maintaining an air gap between the DPF and the digitizers. The coil is protected from electrostatic pickup with a 1 mm thick copper shield and from arcing with 10 layers of 0.003" thick Kapton tape as well as a plastic centering ring.

The MJOLNIR electrodes are made of oxygen-free copper. The five different anodes (Fig. 3) fielded on discharges discussed in this paper are 15 cm (6 inches) or 23 cm (9 inches) in diameter with exposed lengths between 18 cm and 25 cm. The anodes have pre-drilled hollows of radius 3.8, 0.9, or 1.9 cm. The anode-cathode gap is fixed at 4.3 cm. The cathode is comprised of 24 copper rods. The plasma-facing insulator is made of the machinable ceramic MACOR[®] and has an exposed length of 4.6 cm. The MACOR[®] insulator mates to a PEEK base [12] which is not directly exposed to plasma.

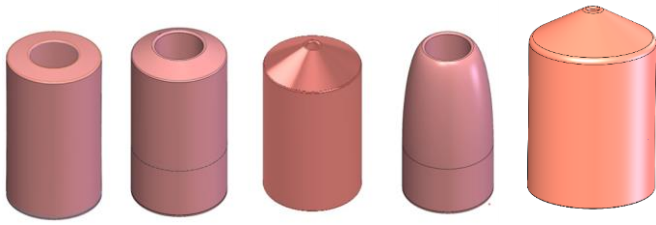


Figure 3: The five MJOLNIR anodes fielded on discharges discussed in this paper, from left to right, A10-3.8-A, A30-3.8-A, A30-0.9-A, P1-3.8, and A15-1.86-30-11.4-A. The “AXX” part of the anode name refers to the taper angle in degrees and the 2nd number in each anode name is the hollow radius in cm. The first 4 anodes are all 15 cm (6”) in outer diameter. The A15-1.86-30-11.4-A anode is 23 cm (9”) in diameter.

Although the anode hollow radius is included in the name of each anode, it is important to note that the implosion radius, the radius at which each anode ceases to taper, is the primary difference between anodes that plays a role in dictating the properties of the implosion [13]. For MJOLNIR anodes fielded thus far, the implosion radius is larger than the hollow radius by approximately 6 mm, due to beveling of the hollow edge.

It is common in the DPF community to quote gas fill densities in units of pressure, meaning the density of fill gas required to produce a particular pressure at room temperature. We follow that convention here and show results from discharges with 8 torr to 24 torr of deuterium gas fill.

B. Particle-in-cell modeling

MJOLNIR discharge simulations are run in the particle-in-cell code CHICAGO™ [14]. The simulations start with the plasma described as a single fluid. Once the plasma reaches the tip of the anode, prior to the start of the final implosion, the simulation is migrated to fully kinetic (electrons and ions) particles, such as in Ref. [7], or to kinetic-ions with inertial-less fluid-electrons. The simulation keeps the kinetic ion description for the remainder of the simulation which typically extends to 100 ns after the ion beam is generated. Cell dimensions are smaller close to the pinch location and larger farther away, typically in the range of 25 to 300 μm . The time step during the fluid stage is 10 ps and decreases to 100 fs prior to the fluid-to-kinetic migration, and is fixed at 100 fs during the kinetic stage. A D-D fusion package [15]

is used to calculate yields from ion interactions. The MJOLNIR pulsed power bank is modelled using the transmission line code BERTHA [16] with lumped circuit parameters of the MJOLNIR towers and the cables. This establishes the boundary conditions between anode and cathode based on a lumped circuit description of the drive and includes finite cable effects. The implicit particle advance uses the direct implicit scheme [17] and collisions are included with a binary method [18, 19].

C. Snow-plow Modeling

In addition to high-fidelity models, our team runs a variety of reduced-order models including a snow-plow model [20] which is used to predict pinch timing based on a lumped circuit driver, gas fill pressure, and charging voltage. The snow-plow model uses a circuit to drive 3 flat pistons which accumulate mass as the gas is swept up. A multiplier on the cross-section-averaged $\mathbf{J} \times \mathbf{B}$ force for the axial piston, unique to each anode shape, is used to achieve correct pinch timing. This multiplier is needed because in the actual device the leading edge of the sheath travels faster than the trailing edge due to the higher magnetic field at the anode. The multiplier is determined by matching timing between the snow-plow model and a CHICAGO simulation for the same anode. Each anode is associated with a single multiplier that reproduces timing at multiple pressures and voltages. The snow-plow model also allows the user to introduce low-inductance alternate current pathways at an arbitrary time, reducing the total load inductance and modifying the modeled current trace.

III. Results and Discussion

In the sections that follow, we outline data and simulation evidence that are consistent with lower-than-expected-yields being caused by parasitic current pathways that divert current away from the main plasma sheath, and slow it down, typically during the implosion but sometimes even earlier, during the run-down.

A. Shape Evolution of DPF Plasma Sheath

Sixteen framing camera pictures from hundreds of DPF discharges have provided a clear pattern of plasma sheath stages. Fig. 4 illustrates these main phases: The first four frames exhibit the plasma sheath during the run-in phase. Then the plasma column pinches and

reaches a minimum radius during the stagnation phase in frame 5. After the stagnation phase, the plasma column begins to expand radially but eventually decelerates against the magnetic field (the 7th frame) due to axial energy and mass flow. At this point the column begins to implode a second time (frames 8-10) although not uniformly due to hydrodynamic instabilities generated during the deceleration process (visible in frame 8) leading to a very structured 2nd stagnation (frame 10). Late in time, the plasma column breaks up or becomes discontinuous (11th and 12th frames).

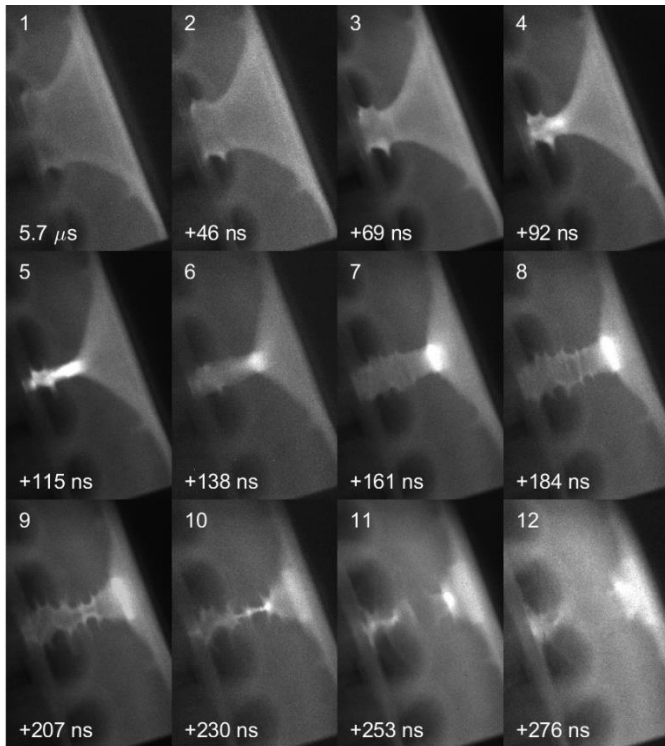


Figure 4: Visible light framing camera images for shot 20190116_0018 demonstrating the typical stages of the plasma sheath shape, from run-in to stagnation, expansion, 2nd compression, and column break-up. Anode A10-3.8-A.

The CHICAGO simulations demonstrate the same phases of plasma sheath shape. Fig. 5 includes simulated ion density plots during the run-in, stagnation, expansion, and break-up. During and after the plasma column break-up, the plasma is no longer effectively conducting current along its entire length, and charge builds up at either end of the breakage. This charge build-up creates electric fields which accelerate ions primarily in the

direction away from the anode (initially around $Z=-1$ cm in Fig. 5) into a dense target that has formed downstream (between $Z=1$ and 2 cm), creating beam-target neutrons. The location of the beam generation has a stochastic component while the target location is primarily determined by the hydrodynamics influenced by the shape of the anode.

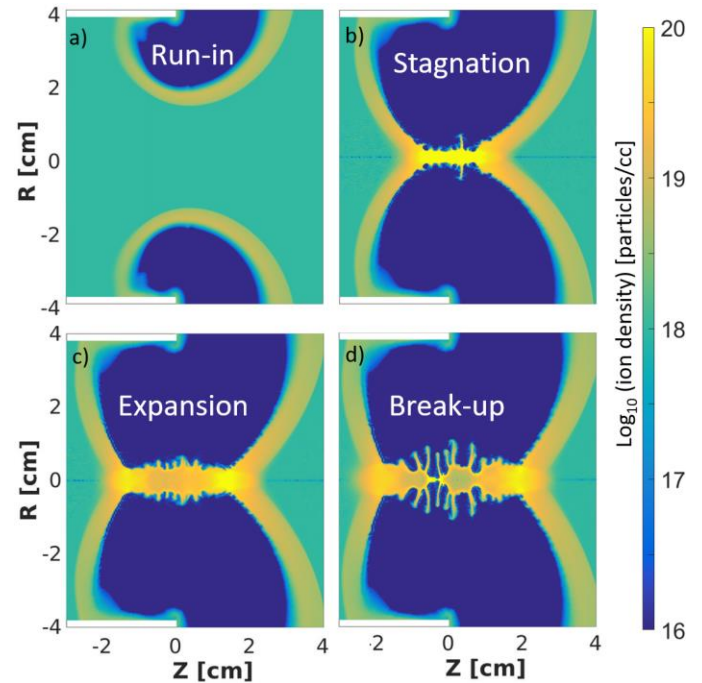


Figure 5: Ion density plots at various stages of the PIC simulations. The discharge goes through a similar series of stages as the experimental framing camera photos: a) run-in, b) stagnation, c) expansion, and d) break-up. Note that half of the simulated pinch region is inside the hollow of the anode, which is not viewable in framing camera images.

B. Stabilization of Run-Down Velocities and Establishment of Nominal Yield

We have observed that several discharges are needed to establish nominal operations after machine assembly and any time new material is introduced in the vacuum chamber. During the first several discharges, the run-down velocities steadily increase until reaching a constant value. Then, the neutron yield will start rising by orders of magnitude for each additional discharge until they reach a nominal value. Because of the stochastic nature of the neutron generation process inside the DPF, the neutron yield will still fluctuate shot-to-shot, even with the same voltage and gas fill pressure, but the

fluctuations are usually within a factor of two of the nominal value.

Run-down speed is expected to scale proportionally to $I/r\sqrt{\rho}$, where I is the current running through the plasma sheath, r is the radius of the plasma sheath (taken to be the anode radius for the fastest part of the sheath during run-down), and ρ is the gas fill mass density. Thus for a fixed electrode geometry, fixed voltage (which determines I), and fixed gas fill pressure (with minimal impurities), we expect a constant run-down speed.

The optical emission of the sheath along certain segments of the anode is used to infer time-averaged plasma sheath run-down velocities Ref [2].

Fig. 6 depicts run-down velocities during a warm-up discharge sequence from April 3rd 2019, in the 1 MJ configuration. Prior to the first discharge, the electrode and insulator hardware had been rebuilt after fixing a vacuum leak. Although run-down velocities stabilize after approximately 5 shots, the neutron yields are increasing monotonically over 10 shots, reaching the highest yield on the final discharge of that day. On the second day, run-down velocity continues to be approximately constant within error bars and yields fluctuate between 1.2×10^{10} and 9.2×10^{10} . Error bars in Fig. 6 only reflect errors that are expected to be random from shot-to-shot so that velocity trends can be assessed relative to error bars. Systematic error due to the location of the light collection nearly doubles the expected error on absolute magnitude of velocity and does not change until the detector is removed.

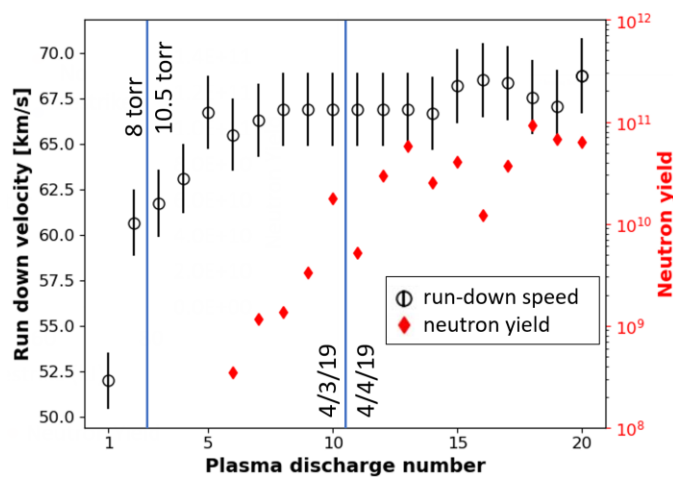


Figure 6: Run-down velocities at $Z=-2.3$ cm as a function of plasma discharge # for April 3-4, 2019 in the 1-MJ configuration. Discharges are at 8 torr/60 kV and 10.5 torr/70 kV (expected to have same sheath velocity to within 2%) on anode A30-3.8-A. Trigger/no plasma shots are left out of the data set. The run-down velocities have stabilized after the first ~5 plasma shots. However, the yield continues to increase over the first 10 or more shots.

Fig. 7 shows a similar sequence for June 21 and 25 of 2019. Prior to June 21, the anode was swapped out during a brief vacuum break. Typical of a shorter vacuum break where little new hardware is introduced in the chamber, in this example the run-down speed stabilizes around the 2nd discharge and yield stabilizes around the 4th discharge. Low initial run-down speeds after a vacuum break could be caused by impurities on the electrodes. During conditioning discharges, these impurities would be expunged by electrode heating and pumped out of the chamber. The theory of impurities poisoning the first few shots is consistent with the observation that more minor hardware change-outs require fewer conditioning shots before nominal run-down speeds and yields are achieved.

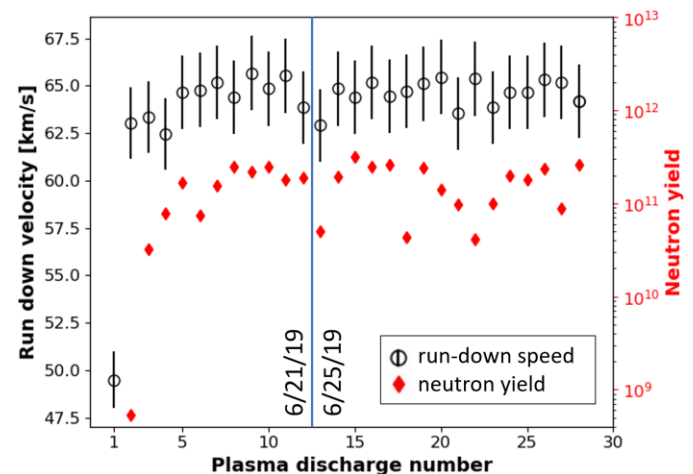


Figure 7: On a simpler rebuild, for example a simple anode swap or window swap, we achieve nominal yields within just a few shots. This series of shots from 6/21/19 and 6/25/19 were taken at 16 torr/90 kV on A30-0.9-A, after an anode swap.

In the 2-MJ configuration, run-down velocities continue to be consistent with one another after conditioning shots. Run-down velocities do not show correlation with neutron yield after initial electrode conditioning. From these two examples and many similar run days, we

conclude that run-down speeds stabilizing is a necessary but not sufficient condition for favorable yield performance.

C. Measured Run-In Velocities for High- and Low-Performing Discharges

We also examine the behavior of run-in speeds and their relationship to yield using framing camera images. An edge-tracking algorithm [2] is used to locate the sheath edge on multiple framing camera images, to infer plasma sheath run-in speeds.

Similarly to the run-down, we expect run-in speeds to scale as $I/r\sqrt{\rho}$, where r is now changing in time as the plasma sheath runs in to smaller radius. Thus, the plasma sheath is now accelerating as a function of time.

The relationship between yield and run-in velocity is illustrated in Fig. 8, which shows the run-in speeds as a function of radial sheath location for four discharges, taken in the 2-MJ configuration at 60 kV and 8 torr fill gas. The higher-yield shots 9 and 10 exhibit higher run-in velocities than the lower-yield shots.

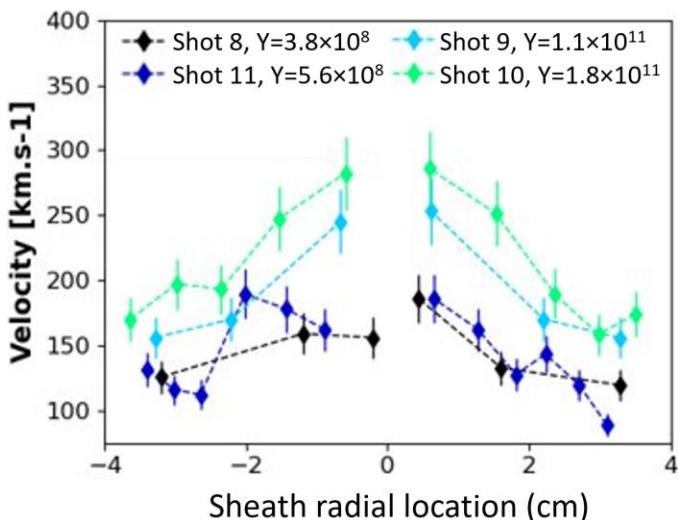


Figure 8: Inferred plasma sheath run-in velocities as a function of sheath radial location for six 60 kV discharges from the 2-MJ configuration at 8 torr fill pressure, taken on 10/29/2020. Low-yield shots have lower measured run-in speeds.

Fig. 9 demonstrates the same trend in a different way, with the several run-in velocities from each discharge distilled into a single representative average velocity over the last 1.5 cm of the run-in.

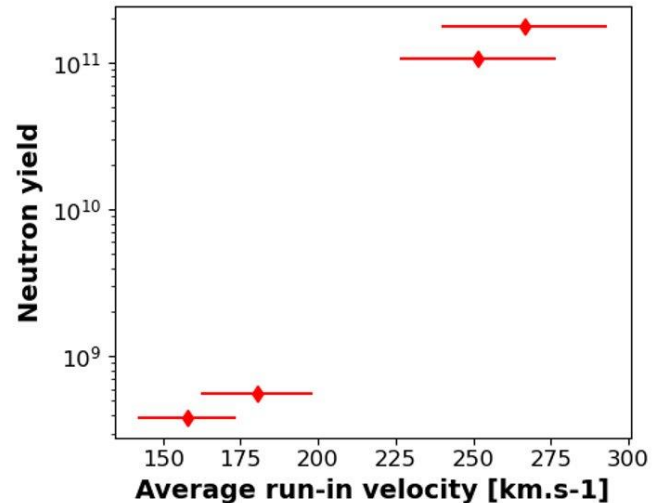


Figure 9: Neutron yields and average run-in velocity for the same sequence of discharges shown in Fig. 10, demonstrating that yields are correlated to run-in speeds.

These slow run-in speeds can be seen in scenarios in which yields are volatile due to known off-normal conditions. On October 29, 2020, MJOLNIR was still recovering from off-normal conditions produced by a shattered tungsten-coated glass slide that was 2 run days previously placed inside the chamber for the purposes of determining vacuum compatibility. The same run-in velocity trend is observed for anomalously low yield “warm-up” shots during electrode conditioning. Due to the plasma sheath’s inertia during run-in, parasitic current paths developing after run-in has started do not easily correlate with neutron yields. We conclude that a stabilization of the run-in velocity is also a necessary but not sufficient condition for high performing discharges.

In principle, slow run-in speeds could be caused by either heavy impurities or by reduced current driving the implosion. In this case the run-down speeds were all very similar, so if impurities were the cause, they would have to be present at the anode tip but not along the length of the anode or cathode.

If the slow speeds are caused by reduced current driving the implosion, one could imagine the pinch region

current lowered by a conducting path that opens up away from the main plasma sheath during the implosion. In the following section, we use a simple snow-plow model to show that measured current traces from low-yield shots exhibit signatures of parasitic current pathways.

D. Effect of Alternate Current Paths on Snow-Plow Model Current Traces

In addition to run-in and run-down velocities, conditioning shots have shown identifiable features on the current traces. Fig. 10 shows the current traces corresponding to the conditioning sequence shown in Fig. 6. We observe that conditioning discharges exhibit a smaller current drop during the implosion than nominal post-conditioning discharges. This could suggest the current is flowing through a lower inductance path than the pinch. To investigate this behavior we used a simple snowplow model.

In order for the snow-plow model to match experimental current traces, an alternate current path must be introduced at some point in time. To match current traces from high-yield discharges, the default alternate current path added to the snow-plow simulation occurs 50 ns after stagnation, introducing a 7 nH conducting path with resistivity 7 m Ω . This is similar to the alternate current paths that appear on their own late in time in the PIC simulations.

However, to match the low- and medium-yield discharges, an initial parasitic current path is added 200 ns and 50 ns *prior* to stagnation, respectively. Thus alternate current paths that occur prior to stagnation are one possible way to explain the lower magnitude “dips” in current on discharges with lower-than-expected yield.

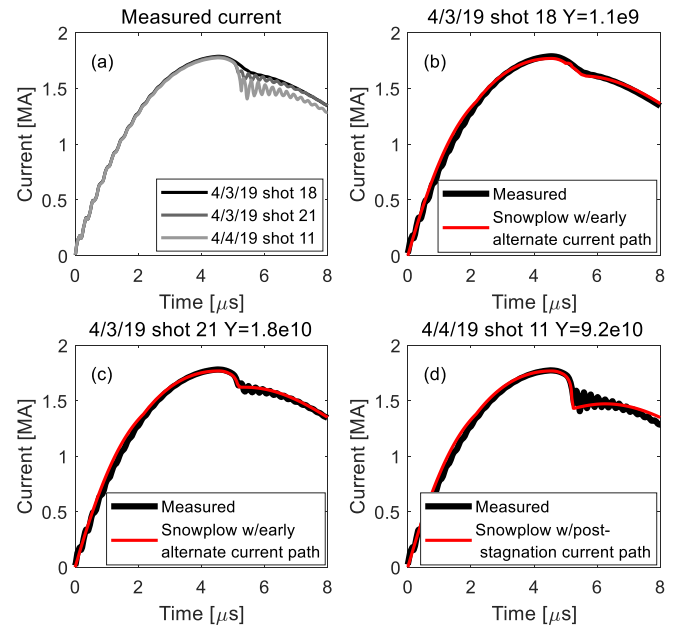


Figure 10: (a) Measured current traces for three discharges corresponding to discharge # 7, 10, and 18 in Fig. 6, with nominally identical starting conditions but very different neutron yields. (b) Measured and snow-plow modeled current traces for discharge corresponding to discharge #7 in Fig. 6, part of the warm-up/conditioning sequence. (c) Measured and snow-plow modeled current traces for discharge corresponding to discharge #10 in Fig. 6, also part of the warm-up/conditioning sequence. (d) Measured and snow-plow modeled current traces for a high-performing discharge corresponding to discharge #18 in Fig. 6. To match the current trace for the high-yield discharge (d), an alternate current path was added 50 ns after stagnation. However, to match the current traces for the two lower-yield shots (b) and (c), alternate current paths had to be added earlier in time, prior to stagnation. Shots were taken at 10.5 torr/70 kV on anode A30-3.8-A.

A smaller current drop during implosion corresponding to a lower yield has not only been observed during conditioning shots, but also during nominal conditions. Fig. 11 illustrates the same analysis for three shots after conditioning had already taken place for the A30-0.9-A anode. This anode, which tapers to a smaller radius before the implosion, exhibits a smaller current dip relative to the A30-3.8-A anode due to more of the load’s final inductance occurring prior to the implosion. In this case, a similar behavior is observed where the parasitic current path is introduced after stagnation to match the high-yield shot’s current trace, at the beginning of the

implosion phase for the medium-yield shot and more than 150 ns prior to implosion for the lowest yield shot.

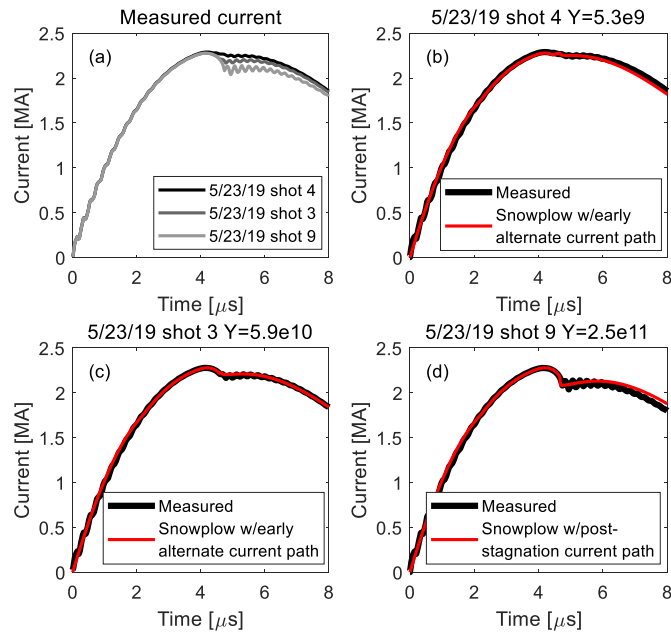


Figure 11: (a) Measured current traces for three discharges during normal operations, after conditioning has already taken place. (b) Measured and snow-plow modeled current traces for the lowest-yield discharge. (c) Measured and snow-plow modeled current traces for the mid-yield discharge. (d) Measured and snow-plow modeled current traces for the highest-yield discharge. The two shots with lower yields can be explained through introduction of parasitic current pathways early in time. The lowest-yield shot required an alternate current pathway prior to implosion in order to match the measured current trace. Shots were taken at 18 torr/90 kV on anode A30-0.9-A.

Another measurement that corroborates the theory of a current path opening up in an alternate location is the voltage probe on the back of the transmission plate, which measures the voltage between anode and cathode. Fig. 12 depicts the anode-cathode voltage for the same three discharges on 5/23/19 whose current traces are in Fig 11. The highest yield discharge reaches a high voltage of approximately 180 kV. The other two discharges also show a rise in voltage during the implosion and generally have a similar voltage trace until about 200 ns prior to maximum voltage on the best-yield shot. At this point, the lowest-yield shot decreases in voltage, an indication that another current path has potentially opened up as a result of the rising voltage.

The timing of the drop in voltage for the lowest yield shot coincides with the time the alternate current path must be introduced in the snow-plow model in order to reproduce the current trace. The same observation is true for the middle-yield shot, which appears to build up a higher voltage prior to opening a new current path.

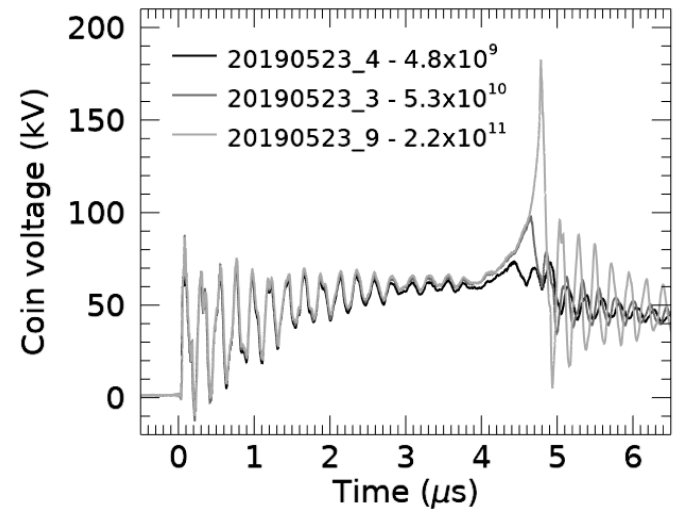


Fig. 12: Voltage measurements from probe on the back of the transmission plate between anode and cathode. The discharge with highest yield exhibits the highest and latest voltage spike. Other discharges' voltage spikes appear to be reduced, likely because the increasing voltage was able to open up a conducting path in those cases, reducing the system voltage. The longer the delay in the opening of a parasitic current path, the higher the voltage achieved.

Fig. 13a shows average dI/dt for a dataset of 48 shots binned into different neutron yield ranges. All shots are 16 torr in the 1-MJ configuration at voltages from 90 to 100 kV. We find that the slope of the current dip is well correlated to neutron yield. In a snow-plow model, the only way for the current trace to flatten is through a decrease in inductance, i.e. another current path opening up. Thus, it appears that much of the seemingly random fluctuations in MJOLNIR neutron yields, even during normal/favorable operations are accompanied by and possibly caused by alternate current paths opening up at random times and locations.

The maximum voltage for each shot on the anode-cathode voltage probe is also correlated to neutron yield, as illustrated in Fig. 13b. Presumably higher neutron yield shots build up a greater voltage across the anode-

cathode, consistent with a delay in the formation of a lower inductance conducting path.

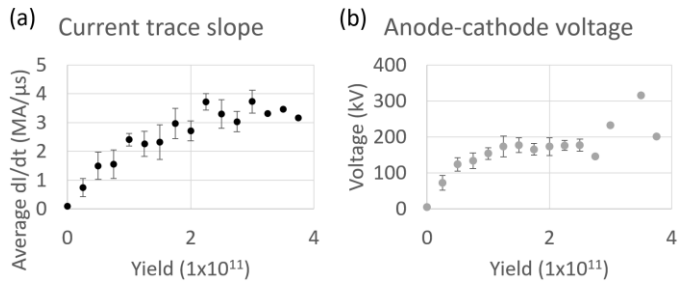


Figure 13: (a) For a dataset of 48 shots at 16 torr, the shot-averaged maximum di/dt as a function of yield. Lower yields shots exhibit less of a current dip, which can only be explained through a decrease in inductance during the implosion. (b) The average of peak voltage reached on a voltage probe across the anode and cathode transmission plates.

In the following section, we use the PIC modeling to better understand how parasitic current pathways might affect beam formation and yield.

E. Effect of Parasitic Current Pathways on Beam Formation and Yield in the PIC Model

In order to understand the potential effect of alternate current paths on the beam formation and neutron yields, we ran PIC models in which we intentionally introduced current either (1) near the insulator or (2) near the tip of the anode in the PIC simulations. The simulations presented were identical and already migrated to kinetic up until the time of the introduction of the alternative current pathway, which was artificially created by making part of the computational grid conducting 100 ns prior to implosion, with a net resistance of 25 m Ω . One additional case was investigated in which the current path near the tip was introduced later in time during the implosion, only 10 ns prior to nominal stagnation time.

Fig. 14 shows values of rB_θ for the three simulation geometries. Constant rB_θ is indicative of no current flowing in a particular region, while changes in rB_θ indicate that current is flowing along rB_θ contours. In Fig. 14a, no alternate current path has been purposefully introduced, and the rB_θ plot indicates that all the current is flowing through the plasma sheath. In Figs. 14b and

14c, alternate current paths have been introduced and the rB_θ plots indicate that some current is now flowing along alternative paths. Note that the total current flowing into the electrodes is actually *higher* for the two shorted geometries because with a lower inductance current path available, the magnitude of the pinch-time current into the electrode is higher. This increased pinch-time current into the electrodes is reflected in the low-magnitude current dips seen on the Rogowski coil measurements in the previous section.

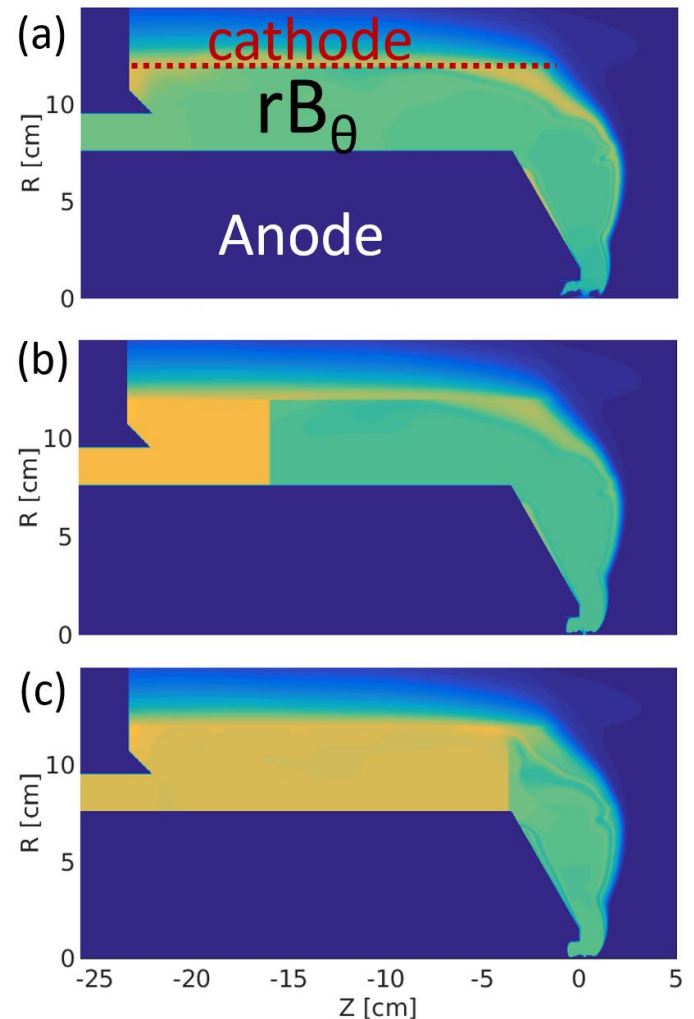


Figure 14: Plots of rB_θ for simulations: (a) in which no alternate current path is purposefully introduced, (b) in which one is intentionally introduced close to the insulator, and (c) in which one is introduced near the tip of the anode. The A30-0.9-A anode geometry is used.

In this set of simulations, we found that neutron yield was highest in the simulation with no intentional alternate current path, followed by a lower yield when the alternate current path was towards the insulator, with the lowest yields obtained when it occurred near the anode tip. The alternate current path near the tip opening up 10 ns prior to stagnation resulted in a more favorable yield than when it opened 100 ns prior to stagnation.

One explanation of the ordering is that a new current path effectively cuts off stored field energy available to convert into beam generation. This is illustrated in Fig. 15 in which the correlation is evident between beam generated in the simulation and magnetic energy available downstream of the parasitic current path.

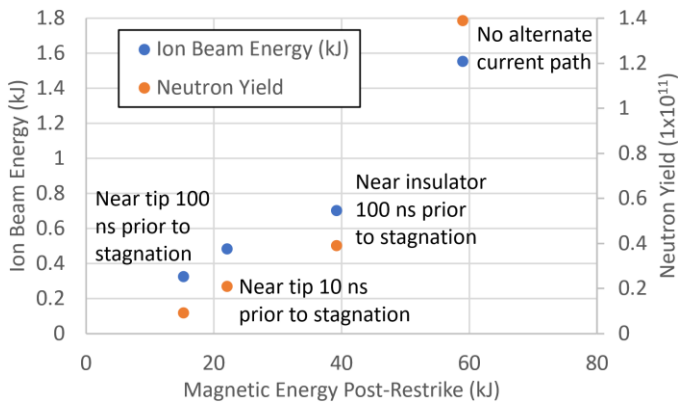


Figure 15: Total ion beam energy in simulations with no parasitic current path, a current path near the insulator (100 ns prior to stagnation), and a current path near the anode tip (10 and 100 ns prior to stagnation). This total ion beam energy correlates well to the magnetic energy existing downstream of the alternate current path.

F. Challenges at Higher Pressures

We initially intended to match MJOLNIR's high currents with high pressures to maximize yield through the formation of high-areal-density targets which could more efficiently convert the ion beam into neutrons. However, we quickly observed that our best yields were at low pressure, and the MJOLNIR neutron yield drops as pressure is increased. We have observed this at many different voltages in both the 1-MJ and 2-MJ

configurations, but we show an illustrative example in Fig. 16a, for the 60 kV setting in the 2-MJ configuration.

It is not immediately obvious that this fall-off in yield at higher pressures is troubling. However, scaling to higher yields at higher current really necessitates being able to operate at high pressures. This is because fundamentally two of the factors of I in the I^4 scaling laws [3, 21] derive from a higher-areal-density target resulting from the higher densities assumed at higher currents; the other two factors of I derive from expected increase in beam quantity. Thus, successful operation at high current but not high pressure will likely at best result in an I^2 scaling.

We posit that poor yields at high pressure are being caused by randomly occurring parasitic current paths that occur more frequently at high pressure. This can be seen by using a metric called dl/dt_{max} , defined by the magnitude of the current trace slope at its steepest descent during the current dip. Fig. 16b shows the fluctuations of this slope by reporting the ratio of the average dl/dt_{max} to the largest dl/dt_{max} observed for a series of shots at 5 different pressures. While the dl/dt_{max} magnitude in current traces is reproducible in low pressure discharges, it becomes more inconsistent as the pressure is increased.

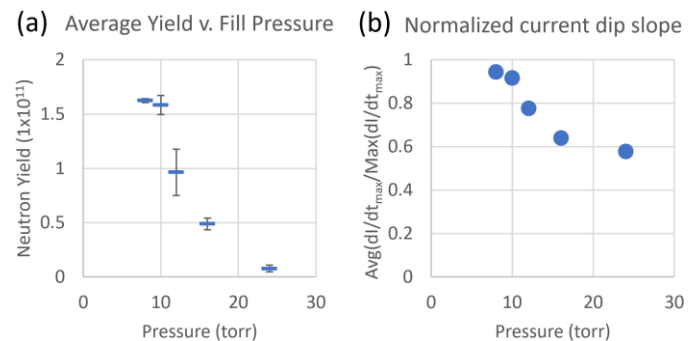


Figure 16: (a) Neutron yield shows clear degradation at higher pressures in the 60 kV/2-MJ configuration and (b) for the same set of shots, the ratio of dl/dt_{max} averaged over all discharges at a given pressure to the largest magnitude dl/dt_{max} for that pressure.

We are exploring several explanations for the increased probability of parasitic current at higher pressure. It may be that higher pressures leave behind a greater residual working gas density in the A-K gap, enabling current to flow in locations other than the plasma sheath. It may be possible to mitigate this effect and maintain I^4 scaling

through the use of a fast rise time gas valve that allows for extra mass on axis while still keeping the rest of the chamber at an 8-10 torr fill. The MJOLNIR team has plans to field these new gas fill configurations after commissioning of the new electrode/insulator assembly.

IV. Conclusion

We investigated the causes of variable neutron yield produced by the MJOLNIR DPF (1) during conditioning, (2) during nominal operations post-conditioning and (3) as a function of pressure. We presented evidence of the existence of parasitic current paths via measurements of slower run down and run-in speeds, lower current dip values, and lower voltage across the anode and cathode transmission plates. Parasitic current paths divert energy away from the pinch region, where neutrons are produced, and are the likely cause of the neutron yield fluctuations.

Immediately following exposure of the vacuum vessel to atmosphere or new hardware in vessel, typical operation in MJOLNIR's 1-MJ and 2-MJ configurations demonstrate run-down speeds, run-in speeds, and yields that tend to stabilize after a few conditioning shots. During off-normal operations or during initial electrode conditioning, when yields fluctuate by more than an order of magnitude, run-in speeds appear to trend with yield, and somewhat constant run-in speeds are obtained when nominal yield is obtained. Yield may continue to fluctuate shot-to-shot by factors of ~ 2 from the average.

Low run-down and run-in speeds could be caused by either (1) the presence of impurities or (2) by alternate current pathways that lessen the magnetic drive in the pinch region during the implosion.

The evidence presented here points to the latter hypothesis. Indeed, snow-plow modeling produces current traces consistent with measured current traces on low-yield shots when a parasitic current pathway is introduced prior to stagnation. Measurements of the anode-cathode voltage across the transmission plates corroborate the snow-plow model by exhibiting a fall in voltage coincident with the timing of the modeled parasitic current pathway. In addition, particle-in-cell simulations indicate that current paths that open during

the implosion limit the amount of field energy available to eventually be converted into beam energy.

Finally, MJOLNIR exhibits lowered yield with increasing pressure. It is difficult to measure run-in speeds on high pressure shots, but consistent with the snow-plow modeling, we posit that parasitic current is also causing the low yields on higher pressure discharges. We observe that the frequency of shots with a reduced (relative to maximum possible) current dip goes up with increasing fill pressure.

Future work is needed to locate alternate current paths in low performing discharges. This includes field-measuring diagnostics such as B-dots and Faraday rotation which are planned for future MJOLNIR campaigns. Optical spectroscopy measurements could also provide some information about impurities present in the implosion region.

We will also further investigate the plasma behavior at higher pressures. We expect to take additional data in these regimes after an upcoming electrode/insulator rebuild. Different configurations of anode shape, AK gap, and cathode length, as well as differential gas fill pressure provided by a gas valve on the anode, may be able to mitigate effects seen so far at high pressures.

Acknowledgements

This work performed under the auspices of the U.S. Department of Energy by Lawrence Livermore National Laboratory (LLNL) under Contract DE-AC52-07NA27344. Computing support for this work came from the LLNL Institutional Computing Grand Challenge program.

References

- [1] J.W. Mather. "Investigation of the High-Energy Acceleration Mode in the Coaxial Gun." *Physics of Fluids* 7, S28 (1964). <https://doi.org/10.1063/1.1711086>
- [2] A. Schmidt, E. Anaya, M. Anderson, J. Angus, S. Chapman, C. Cooper, O. Drury, C. Goyon, S. Hawkins, D.P. Higginson et al, "First Experiments and Radiographs on the MegaJoule Neutron Imaging Radiography (MJOLNIR) Dense Plasma Focus," *IEEE Transactions on*

Plasma Science, v 49 (2021) pg 3299-3306.

<https://doi.org/10.1109/TPS.2021.3106313>

[3] B. Bures and M. Krishnan. "An alternative scaling model for neutron production in Z-pinch devices."

Physics of Plasmas, v 19, 112702 (2012).

<http://dx.doi.org/10.1063/1.4764894>

[4] A. Schmidt, V. Tang, D. Welch. "Fully Kinetic Simulations of Dense Plasma Focus Z-Pinch Devices."

Physical Review Letters, v 109 (2012): 205003.

<https://doi.org/10.1103/PhysRevLett.109.205003>

[5] A. Schmidt, A. Link, D. Welch, V. Tang, J. Ellsworth, S. Falabella. "Comparisons of Dense Plasma Focus Kinetic Simulations with Experimental Measurements." Physical Review E, v89 (2014): 061101.

<http://dx.doi.org/10.1103/PhysRevE.89.061101>

[6] A. Schmidt, A. Link, D. Welch, T. Meehan, V. Tang, C. Halvorson, M. May, E.C. Hagen. "Fully Kinetic Simulations of MegaJoule-Scale Dense Plasma Focus." Physics of Plasmas, v 21 (2014): 102703.

<http://dx.doi.org/10.1063/1.4897192>

[7] S. Jiang, D. Higginson, A. Link, I. Holod, A. Schmidt. "Effect of polarity on beam and plasma target formation in a dense plasma focus." Physics of Plasmas, v 26 (2019); 042702.

<https://doi.org/10.1063/1.5048423>

[8] H. Herold, A. Jerzykiewicz, M. Sadowski, and H. Schmidt, "Comparative analysis of large plasma focus experiments performed at IPF, Stuttgart, and IPJ, Świerk," Nuclear Fusion 29 1255 (1989).

<https://doi.org/10.1088/0029-5515/29/8/002>

[9] R. A. Cooper, F. W. MacDougall, J. B. Ennis, J. C. Cochrane, W. A. Reass and W. M. Parsons, "High energy, low inductance, high current fiberglass energy storage capacitor for the Atlas Machine Marx modules," Digest of Technical Papers. 12th IEEE International Pulsed Power Conference. (Cat. No.99CH36358), Monterey, CA, USA, 1999, pp. 122-125 vol.1.

<https://doi.org/10.1109/PPC.1999.825427>

[10] W. M. Parsons, E.O. Ballard, R.R. Bartsch, J.F. Benage, G.A. Bennett, R.L. Bowers, D.W. Bowman, J.H. Brownell, J.C. Cochrane, H.A. Davis et al, "The Atlas project-a new pulsed power facility for high energy

density physics experiments," in IEEE Transactions on Plasma Science, vol. 25, no. 2, pp. 205-211, April 1997.

<https://doi.org/10.1109/27.602492>

[11] R. E. Reinovsky, W. L. Atchison, G. Dimonte, A. M. Kaul, G. Rodriguez, C. L. Rousculp, P. T. Reardon; P. Turchi, "Pulsed-Power Hydrodynamics: An Application of Pulsed-Power and High Magnetic Fields to the Exploration of Material Properties and Problems in Experimental Hydrodynamics," in IEEE Transactions on Plasma Science, vol. 36, no. 1, pp. 112-124, Feb. 2008.

<https://doi.org/10.1109/TPS.2007.914708>

[12] US patent 10978225

<https://www.osti.gov/doi/patents/biblio/1823845>

[23] J. Angus, A. Link, A. Schmidt. "One-dimensional theory and simulations of the dynamic Z-pinch." Physics of Plasmas, v 27 (2020); 012108.

<https://doi.org/10.1063/1.5104340>

[14] C. Thoma, D. R. Welch, R. E. Clark, D. V. Rose, and I. E. Golovkin, Phys. Plasmas 24 062707 (2017).

<https://doi.org/10.1063/1.4985314>

[15] D.P. Higginson, A. Link, A. Schmidt. "A pairwise nuclear fusion algorithm for weighted particle-in-cell plasma simulations." Journal of Computational Physics, v 388 (2019); 439.

<https://doi.org/10.1016/j.jcp.2019.03.020>

[16] D. D. Hinshelwood NRL Memorandum Report 5185, Nov. 21 1983, Naval Research Laboratory.

<https://www.osti.gov/biblio/5610957-bertha-versatile-transmission-line-circuit-code>

[17] B. I. Cohen, A. B. Langdon, and A. Friedman, Journal of Computational Physics 46, 15 (1982).

[https://doi.org/10.1016/0021-9991\(82\)90002-X](https://doi.org/10.1016/0021-9991(82)90002-X)

[18] K. Nanbu, "Theory of cumulative small-angle collisions in plasmas," Physical Review E v 55, 4642 (1997).

<https://doi.org/10.1103/PhysRevE.55.4642>

[19] D.P. Higginson, I. Holod, A. Link, "A Corrected Method for Coulomb Scattering in Arbitrarily Weighted Particle-in-Cell Plasma Simulations" J. Comput. Phys. 413, 109450 (2020).

<https://doi.org/10.1016/j.icp.2020.109450>

[20] V. Tang, M. L. Adams and B. Rusnak, "Dense Plasma Focus Z-Pinches for High-Gradient Particle Acceleration," in IEEE Transactions on Plasma Science, vol. 38, no. 4, pp. 719-727, April 2010, doi: 10.1109/TPS.2009.2037504.

<https://doi.org/10.1109/TPS.2009.2037504>

[21] Lee, S., Saw, S.H. "Neutron Scaling Laws from Numerical Experiments." Journal of Fusion Energy 27, 292–295 (2008).

<https://doi.org/10.1007/s10894-008-9132-7>